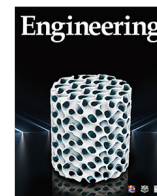




Contents lists available at ScienceDirect

Engineering

journal homepage: www.elsevier.com/locate/eng

Research
Frontiers of Chemical Engineering—Article

Heteropolyacids-Immobilized Graphitic Carbon Nitride: Highly Efficient Photo-Oxidation of Benzyl Alcohol in the Aqueous Phase

Lifu Wu, Sai An*, Yu-Fei Song*

State Key Laboratory of Chemical Resource Engineering, Beijing Advanced Innovation Center for Soft Matter Science and Engineering, Beijing University of Chemical Technology, Beijing 100029, China

ARTICLE INFO

Article history:

Received 17 November 2019

Revised 3 July 2020

Accepted 3 July 2020

Available online xxxx

Keywords:

Photocatalysis
Heteropolyacids
Graphitic carbon nitride
Benzaldehyde

ABSTRACT

Benzaldehyde is a highly desirable chemical due to its extensive application in medicine, chemical synthesis and food sector among others. However, its production generally involves hazardous solvents such as trifluorotoluene or acetonitrile, and its conversion, especially selectivity in the aqueous phase, is still not up to expectations. Hence, developing an environmentally benign, synthetic process for benzaldehyde production is of paramount importance. Herein, we report the preparation of a photocatalyst (PW₁₂-P-UCNS, where PW₁₂ = H₃PW₁₂O₄₀·xH₂O and P-UCNS = phosphoric acid-modified unstack graphitic carbon nitride) by incorporating phosphotungstic acid on phosphoric acid-functionalised graphitic carbon nitride (g-C₃N₄) nanosheets. The performance of PW₁₂-P-UCNS was tested using the benzyl alcohol photo-oxidation reaction to produce benzaldehyde in H₂O, at room temperature (20 °C). The as-prepared PW₁₂-P-UCNS photocatalyst showed excellent photocatalytic performance with 58.3% conversion and 99.5% selectivity within 2 h. Moreover, the catalyst could be reused for at least five times without significant activity loss. Most importantly, a proposed Z-scheme mechanism of the PW₁₂-P-UCNS-catalysed model reaction was revealed. We carefully investigated its transient photocurrent and electrochemical impedance, and identified superoxide radicals and photogenerated holes as the main active species through electron spin-resonance spectroscopy and scavenger experiments. Results show that the designed PW₁₂-P-UCNS photocatalyst is a highly promising candidate for benzaldehyde production through the photo-oxidation reaction in aqueous phase, under mild conditions.

© 2020 THE AUTHORS. Published by Elsevier LTD on behalf of Chinese Academy of Engineering and Higher Education Press Limited Company. This is an open access article under the CC BY-NC-ND license (<http://creativecommons.org/licenses/by-nc-nd/4.0/>).

1. Introduction

Aromatic aldehydes such as benzaldehydes are essential and highly desirable fine chemicals due to their wide applicability [1]. Industrially, benzaldehyde can be obtained by the chlorination of toluene and subsequent saponification [2]. This, synthetic process generally employs the use of potent oxidants like Cr^{VI}, ClO⁻, Br₂, or peroxy acids, leading to the over-oxidation of target product and thereby its poor selectivity. Nowadays, with the increasingly prominent environmental and energy problems, and the continuous requests for improvement of industrial processes with energy-extensive coconsumption, laborious post-treatment and difficult separation, such as benzaldehyde production, there is an

urgent need to develop environmentally-benign, synthetic processes.

Recently, photocatalysis, which is considered a promising and green strategy, has drawn the attention of researchers towards driving chemical reactions to produce valuable compounds [3,4]. Compared with traditional heating treatment, the utilisation of solar power can be a potential energy-source for industrial production processes, as it allows for energy conservation and environmental protection. Therefore, based on the principles of green and sustainable chemistry, the selective conversion process of benzyl alcohol to produce benzaldehyde using semiconductors, can be considered as one of the most promising ways. So far, multifarious semiconductors, i.e. metal oxides, nitrides, sulfides, etc. have been used for the oxidation reaction of benzyl alcohol [1,4–8]. Unfortunately, most of them suffer from high production cost, environmentally hostile production processes, and poor selectivity. As such, it is highly challenging to design a novel and economical

* Corresponding authors.

E-mail addresses: ansai@mail.buct.edu.cn (S. An), songyf@mail.buct.edu.cn (Y.-F. Song).

<https://doi.org/10.1016/j.eng.2020.07.025>

2095-8099/© 2020 THE AUTHORS. Published by Elsevier LTD on behalf of Chinese Academy of Engineering and Higher Education Press Limited Company. This is an open access article under the CC BY-NC-ND license (<http://creativecommons.org/licenses/by-nc-nd/4.0/>).

photocatalyst for efficient synthesis of benzaldehyde in aqueous phase. Graphitic carbon nitride ($g\text{-C}_3\text{N}_4$) has excellent characteristics, such as stable physicochemical properties, nontoxicity, and a suitable band gap (2.7 eV) for the absorption of UV-visible light. Moreover, it can be obtained from various abundant and inexpensive feedstocks, such as cyanamide, urea, melamine, and thiourea. However, significant decrease of photocatalytic activity is usually reported for $g\text{-C}_3\text{N}_4$ due to the rapid recombination of photogenerated electrons and holes (e_{CB}^- and h_{VB}^+), which significantly decreases the photocatalytic efficiency. The aforementioned drawback can be effectively settled by coupling with various semiconductors [9].

Polyoxometalates (POMs) are composite of transition metal oxide clusters, which are a huge and rapidly expanding family. Due to POMs' unique chemical structures and numerous characteristics in accordance with semiconductor metal oxide clusters, they are generally regarded as the analogs of the latter and exhibit excellent photochemical performance in various chemical reactions [5]. Upon irradiation with light energy, the surface of photocatalyst can trap the photogenerated electrons and holes, and thereby the reactive oxygen species of $\cdot\text{O}_2^-$ or/and $\cdot\text{OH}$ radicals are formed to facilitate the photocatalytic reaction. Since the photocatalytic oxidation reaction of benzyl alcohol under solar light irradiation was reported using a POMs catalyst ($[\text{S}_2\text{W}_{18}\text{O}_{62}]^{4-}$) [10], the unique charms of POMs in photocatalytic synthesis of chemicals with high added value, especially aromatic aldehydes, were discovered [5,11].

Herein, we report for the first time the fabrication of a heterogeneous photocatalyst ($\text{PW}_{12}\text{-P-UCNS}$; where PW_{12} is $\text{H}_3\text{PW}_{12}\text{O}_{40}\cdot x\text{H}_2\text{O}$ and P-UCNS is phosphoric acid-modified unstack $g\text{-C}_3\text{N}_4$) by immobilising phosphotungstic acid onto a $g\text{-C}_3\text{N}_4$ surface modified with phosphoric acid. This photocatalyst is applied in a green photocatalytic reaction system, for selective photo-oxidation to produce benzaldehyde in aqueous phase. The as-prepared $\text{PW}_{12}\text{-P-UCNS}$ exerted outstanding photocatalytic oxidation performance, attributed to three factors. Firstly, the incorporated POMs acted as superior electron acceptors to curb the recombination of photogenerated electrons and holes. Secondly, the P-UCNS with phosphoric acid-modified surface improved the absorption of O_2 to generate more active species ($\cdot\text{O}_2^-$ radicals). Thirdly, the interfacial photogenerated electrons within $\text{PW}_{12}\text{-P-UCNS}$ followed a Z-scheme mechanism, which obtained an efficient charge separation by the fast transfer pathway. Moreover, the high oxidation activity and reusability of the $\text{PW}_{12}\text{-P-UCNS}$ photocatalyst revealed a broad and promising application prospects.

2. Experimental section

2.1. Chemicals and reagents

All solvents and chemicals were provided from Energy Chemical (China), were of analytical grade, and were used without further treatment.

2.2. Fabrication of UCNS

Bulk $g\text{-C}_3\text{N}_4$ was synthesised according to Ref. [12]. A quantity of 0.9 g of bulk $g\text{-C}_3\text{N}_4$ was dispersed into 150 mL HCl solution (14.8 wt%) followed by sonicating for 1 h and stirring for another 24 h. Subsequently, it was subjected hydrothermal treatment at 110 °C. After 5 h, the suspension was centrifuged, filtrated, washed with water, and finally dried at 80 °C overnight, leading to the formation of unstack $g\text{-C}_3\text{N}_4$ nanosheets (UCNS).

2.3. Fabrication of $\text{PW}_{12}\text{-P-UCNS}$

As shown in Fig. 1, 0.1 g UCNS was scattered in 100 mL of 0.3 mol·L⁻¹ H_3PO_4 solution and the above was stirred for 5 h to allow for adsorption of phosphoric acid on the surface of UCNS. The P-UCNS was collected by centrifugation. After heating at 60 °C in an oven for 180 min, it underwent heat-treatment at 300 °C for 90 min. P-UCNS was washed using distilled water and then dried, in order to remove weakly bound phosphoric acid anions from its surface [13]. Subsequently, predetermined quantity of $\text{H}_3\text{PW}_{12}\text{O}_{40}$ (PW_{12}) was placed in a 20 mL P-UCNS suspension of anhydrous ethanol, followed by stirring. After drying overnight, the $\text{PW}_{12}\text{-P-UCNS}$ photocatalyst was finally obtained.

2.4. Characterisation

Transmission electron microscopy (TEM) was performed using a HT7700 machine. A Shimadzu XRD-6000 diffractometer was used to collect the X-ray diffraction (XRD) patterns within the range of 3°–70°. A Bruker Vector 22 infrared spectrometer was employed to collect Fourier transform infrared spectroscopy (FT-IR) spectra within the range of 400–4000 cm⁻¹. Thermogravimetric analysis (TGA) was conducted using a TGA/DSC 1 machine with small furnace (SF; temperature range to 1100 °C) from METTLER TOLEDO, USA, under nitrogen atmosphere. X-ray photoelectron spectroscopy (XPS) was conducted using a Quantera SXM machine from ULVAC-PHI Inc., Japan. High-resolution transmission electron microscopy (HRTEM) was carried out using a JEM-2010 electron microscope (JEOL Ltd., Japan). Porosimetry analysis was conducted using a ASAP 2020M machine (Micromeritics Instrument Corporation, USA).

2.5. Performance tests

The photocatalytic performance of as-prepared $\text{PW}_{12}\text{-P-UCNS}$ was systematically investigated using benzyl alcohol photo-oxidation as a model reaction to synthesis benzaldehyde under Xe light (300 W) at room temperature. Firstly, 20 mg of the prepared catalyst was scattered into 10 mL reactants solution (10 mmol·L⁻¹). Before light illumination, the reactive system was placed in the dark for 30 min with continuous stirring, in order to reach the adsorption-desorption equilibrium between reactants and the catalyst. Subsequently, oxygen was bubbled into the mixture and sustained for 2 h. After irradiation, an 1 mL mixture was taken out, followed by centrifugation and filtration to separate the photocatalyst. Gas chromatography was employed using GC-2010 Pro (with HP-5 chromatographic column: inner diameter = 0.25 mm, length = 30 m; Shimadzu Corporation, Japan), to analyse and identify the products, using cyclooctane as an internal standard, and thus calculate the benzyl alcohol conversion and benzaldehyde selectivity.

2.6. Photoelectrochemical tests

Experiments were conducted on a typical CHI 760E electrochemical workstation (CH Instruments, Inc., USA), using a 300 W Xe lamp as a light source. Photocurrent analysis was conducted in Na_2SO_4 solution (0.1 mol·L⁻¹) by selecting Ag/AgCl and Pt wire as the reference and counter electrode, respectively. Working electrodes were prepared as follows: 5 mg catalyst was suspended in 1 mL of ethanol solution using ultrasonication. 80 μL of the above slurry was coated on an ITO substrate and left to dry. The cyclic voltammogram (CV) plot and Mott-Schottky measurements were conducted as shown in previous work [1,12].

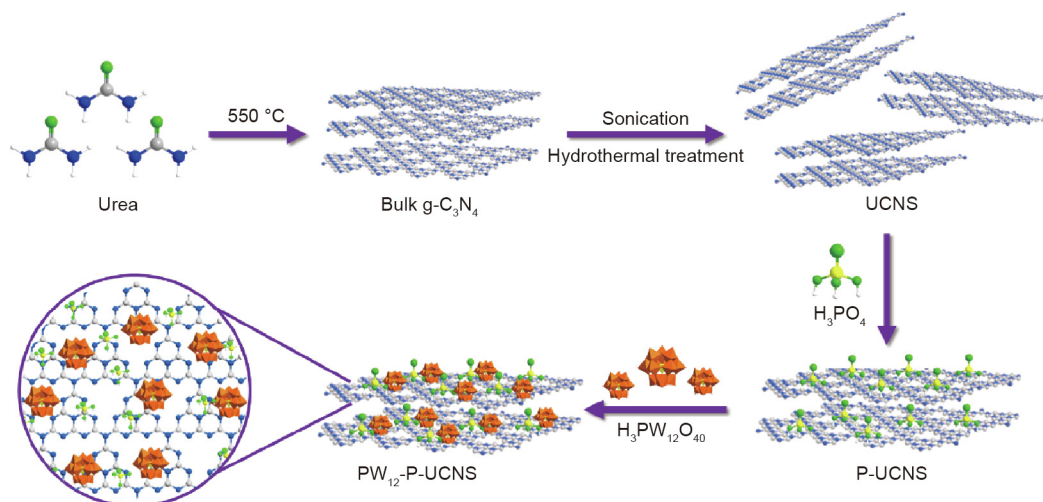


Fig. 1. Illustrated representation of the synthetic process for the $\text{PW}_{12}\text{-P-UCNS}$.

3. Results and discussion

3.1. Synthesis of catalysts

As shown in Fig. 1, the $\text{PW}_{12}\text{-P-UCNS}$ was successfully fabricated using hydrothermal treatment and an immersion process. Briefly, bulk $\text{g-C}_3\text{N}_4$ was obtained by firstly treating it with urea at 550 °C. Then, $\text{g-C}_3\text{N}_4$ was exfoliated via a HCl-assisted hydrothermal treatment and sonication. The above powder was further modified by phosphoric acid and $\text{PW}_{12}\text{-P-UCNS}$ was finally prepared after the incorporation of PW_{12} . During the preparation of the $\text{PW}_{12}\text{-P-UCNS}$, the $-\text{NH}_2$ groups from the edges of P-UCNS were protonated by the acid to form $[-\text{NH}_3^+][\text{H}_2\text{PW}_{12}\text{O}_{40}^-]$ species at the interface between PW_{12} and P-UCNS. The leakage of the Keggin structure can be avoided due to the strong bonding of PW_{12} and P-UCNS via acid-base and electrostatic interaction. Moreover, the incorporation of PW_{12} accelerates the transfer and separation of charge carriers.

3.2. Compositional and structural information

As shown in Fig. 2, the XRD patterns can be used to characterise the chemical structure of bulk $\text{g-C}_3\text{N}_4$, UCNS, P-UCNS, PW_{12} , and $\text{PW}_{12}\text{-P-UCNS}$. The two broad peaks positioned at 27.5° and 13.0°, on the bulk $\text{g-C}_3\text{N}_4$ spectra are matched to (002) and (100) of the graphitic carbon materials, respectively [12,14]. The slight shift of (002) peak for the UCNS and P-UCNS compared with bulk

$\text{g-C}_3\text{N}_4$, is attributed to the protonation of heterocyclic N atoms (C-N=C) [15–17]. Moreover, it can be seen that the shifts of P-UCNS in higher 2θ angles are due to the lower extent of stacking between nanosheets [18,19]. For as-prepared $\text{PW}_{12}\text{-P-UCNS}$, it shows that the characteristic peaks of the Keggin structure (2θ of 8°–11° and 18°–30°) and P-UCNS (at 2θ of 14° and 28.2°) in the XRD diagram, indicating that the structures of Keggin units and P-UCNS supports are remained after the incorporation of PW_{12} .

Further, structural information of as-prepared $\text{PW}_{12}\text{-P-UCNS}$ was obtained through FT-IR measurement. Typically, $\text{g-C}_3\text{N}_4$ shows peaks centered at 890 and 810 cm^{-1} , attributed to the breathing mode of the heptazine ring (Fig. 2(b)) [20]. The signals centered at 1637, 1570, and 1463 cm^{-1} can be attributed to the $\nu_{\text{C-N}}$, while the peaks observed at 1416 cm^{-1} can be assigned to $\nu_{\text{C=N}}$ [21,22]. Moreover, the signals appearing at 1248, and 1327 cm^{-1} can be assigned to the $\nu_{\text{C-NH-C}}$ or $\nu_{\text{C-N(C)-C}}$ [17,23]. The broad peaks centered at the range of 3000 to 3500 cm^{-1} can be assigned to the $\nu_{\text{O-H}}$ and $\nu_{\text{N-H}}$, [24,25]. For UCNS and P-UCNS, the signals at 1463 and 1637 cm^{-1} (assigned to C=N and C-N respectively) shift to 1466 and 1639 cm^{-1} , respectively. In addition, the peak positioned at 1570 cm^{-1} , ascribed to C=N in the CN heterocycles, becomes inconspicuous, implying that $\text{g-C}_3\text{N}_4$ were protonated successfully [15,26,27]. The new signal observed at 985 cm^{-1} in the P-UCNS spectrum, corresponds to the phosphoric acid groups [28]. The FT-IR spectrum of PW_{12} shows characteristic vibration peaks at 1080, 984, 890, and 798 cm^{-1} , respectively [29]. All of the characteristic

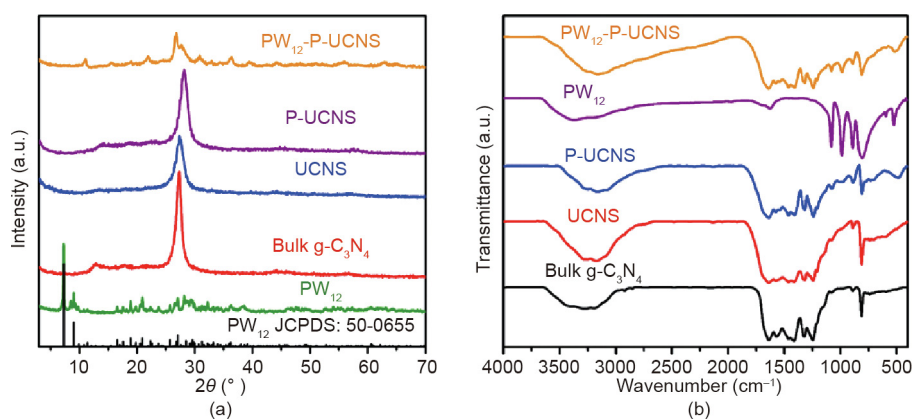


Fig. 2. The (a) XRD and (b) FT-IR for different specimens (UCNS, P-UCNS, bulk $\text{g-C}_3\text{N}_4$, PW_{12} , and $\text{PW}_{12}\text{-P-UCNS}$). JCPDS: Joint Committee on Powder Diffraction Standards.

peaks for PW_{12} and P-UCNS mentioned so far can also be observed in the spectrum of PW_{12} -P-UCNS. Therefore, the above results indicate that ① the $g-C_3N_4$ successfully transforms to P-UCNS after exfoliating, protonating, and modifying by phosphoric acid; ② PW_{12} is successfully incorporated on the P-UCNS surface; ③ the primary Keggin structure of PW_{12} remains intact after immobilisation.

The PW_{12} -P-UCNS photocatalyst was also analysed using XPS. Peaks for P, O, N, W and C elements are clearly detected for PW_{12} -P-UCNS (Fig. 3(a)). The C 1s XPS spectrum of the PW_{12} -P-UCNS (Fig. 3(b)), can be divided into four signals centered at 289.2, 288.0, 286.0, and 284.8 eV. The peaks centered at 288 and 284.8 eV are attributed to the $N=C(-N)_2$ unit and reference C species, respectively [16,30,31]. The peaks originated from C species of C-O and C-NH₂ groups can be found at 289.2 and 286.0 eV. In the N 1s spectrum (Fig. 3(c)), the four peaks located at 404.0, 400.2, 399.1, and 398.2 eV are attributed to the C-NH⁺=C, C-N-H or N-H₂ groups, N-(C)₃ and sp² hybridised C-N=C groups respectively [32–35]. Moreover, it is clear that the N 1s and C 1s spectra of PW_{12} -P-UCNS show an obvious shift, compared with UCNS and P-UCNS due to the protonation and strong electrostatic interaction of the PW_{12} species [13,17,29]. The W 4f XPS spectrum of the PW_{12} -P-UCNS (Fig. 3(d)) shows that it is divided into two signals centered at 37.4 and 35.3 eV, ascribing to the W 4f_{5/2} and W 4f_{7/2} spin-orbit components accordingly, indicating the W^{VI} species of the incorporated PW_{12} [36]. Moreover, the negative shifts of the binding energy that can be observed compared with the PW_{12} spectrum (W 4f_{5/2} of 37.9 eV and W 4f_{7/2} of 35.8 eV), can be explained through the chemical interaction between P-UCNS and the Keggin units [37].

3.3. Morphological characteristics and textural properties

The morphology of PW_{12} -P-UCNS was investigated using TEM and was compared with $g-C_3N_4$, UCNS, and P-UCNS. As shown in

Fig. 4, all the prepared materials show layered nanostructures. Compared with $g-C_3N_4$, which shows thick and blocky nanostructure (~29 nm for thickness, in Appendix A. Fig. S1), the as-prepared PW_{12} -P-UCNS exhibits extremely thin nanosheets (~12 nm for thickness, Fig. S1). The open-up surface provides abundant active sites and shorter diffusion distances, is conducive to accelerate charge separation and mass transfer, and thereby leads to enhanced photo-oxidation activity of PW_{12} -P-UCNS [38]. Moreover, it can be seen that the thickness of UCNS rapidly decreases to 10 nm following the hydrothermal treatment of $g-C_3N_4$, and it almost remains after the incorporation of phosphoric acid and POMs. This observation is consistent with the result obtained from atomic force microscopy (AFM). Closer inspection of the HRTEM images (Fig. S2) shows that the prepared PW_{12} -P-UCNS is well-defined with uniformly dispersed black spots. This is in agreement with the dimensions of the PW_{12} clusters, and suggests that the clusters are uniformly incorporated on P-UCNS. Furthermore, the as-prepared UCNS, P-UCNS, and PW_{12} -P-UCNS exhibit porous nanostructures, as revealed by the measurement of porosity (Fig. S3).

3.4. Optical absorption properties

The energy band features and optical absorption properties of UCNS, $g-C_3N_4$, P-UCNS and PW_{12} -P-UCNS are discussed based on the obtained UV-visible diffuse reflectance spectra (UV-Vis/DRS). In Fig. 5, the absorption region of PW_{12} is within the area of 200 to 422 nm, attributed to the charge transfer from O 2p to W 5d orbit at W=O and W-O-W, respectively [12]. Moreover, it can be observed that the absorption edge of other materials ends up in the scope of 440–480 nm because of the electron transition from the valence band (VB) contributed by N 2p to the conduction band (CB) contributed by C 2p orbitals [39]. Furthermore, the absorption

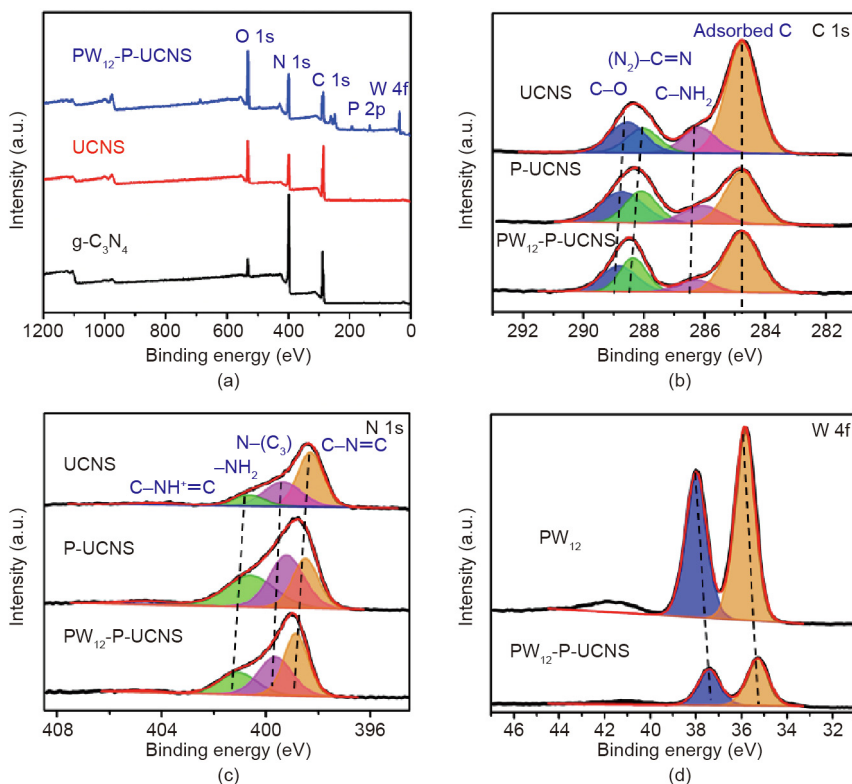


Fig. 3. (a) XPS survey of different samples (PW_{12} -P-UCNS, $g-C_3N_4$, and UCNS); XPS spectra of the (b) C 1s, (c) N 1s of UCNS, P-UCNS, and PW_{12} -P-UCNS, and (d) W 4f for PW_{12} and PW_{12} -P-UCNS.

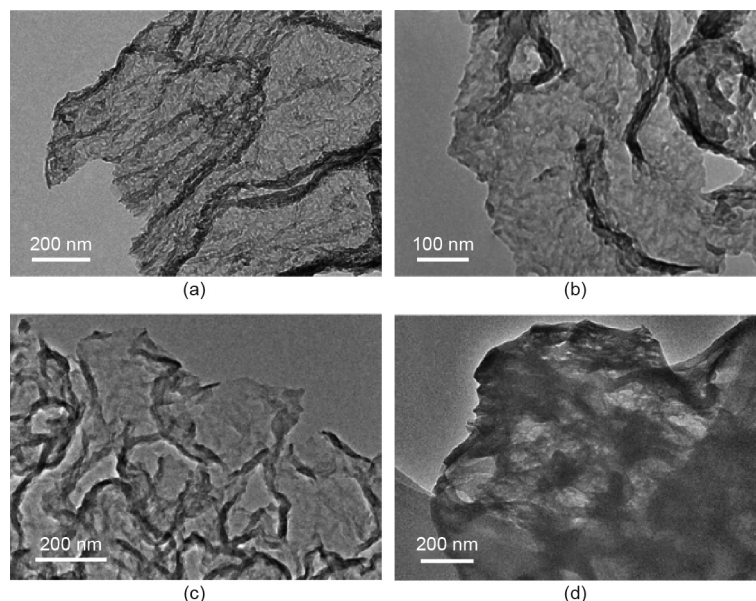


Fig. 4. TEM of (a) PW_{12} -P-UCNS, (b) P-UCNS, (c) UCNS, and (d) bulk $\text{g-C}_3\text{N}_4$.

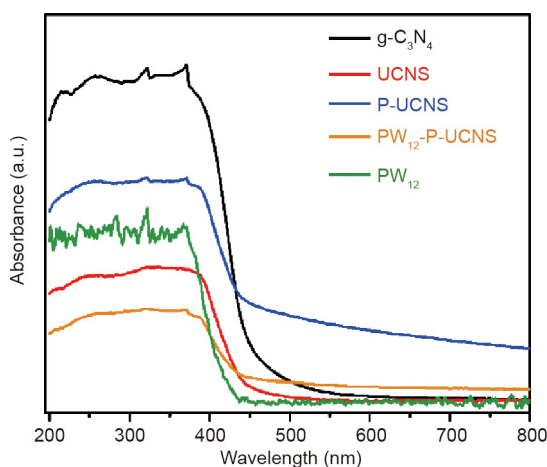


Fig. 5. UV-Vis/DRS plots of different samples ($\text{g-C}_3\text{N}_4$, UCNS, P-UCNS, PW_{12} , and PW_{12} -P-UCNS).

peak associated with PW_{12} or P-UCNS could not be observed in the spectra of PW_{12} -P-UCNS (Fig. 5), indicating that the incorporated PW_{12} is uniformly dispersed throughout the whole composite [13]. According to the plots of $(\alpha h\nu)^{1/2}$ vs. photon energy ($h\nu$) of Fig. S4, the band gap (E_g) of various materials can be estimated from Tauc plots expressed by $(\alpha h\nu)^{1/2} = A(h\nu - E_g)$, where ν , E_g , A , and α are the frequency of light, the energy of band gap, proportionality constant, and absorption modulus, respectively [40,41]. The E_g of PW_{12} , $\text{g-C}_3\text{N}_4$, UCNS, and P-UCNS are 2.80, 2.62, 2.69, and 2.42 eV, respectively. Comparing with $\text{g-C}_3\text{N}_4$ and UCNS, the blue shift of the band gap energy proves that the light absorption capacity of P-UCNS is improved.

3.5. Performance studies

In order to test the performance of PW_{12} -P-UCNS, the oxidation reaction of benzyl alcohol under Xe lamp illumination was chosen. For comparison, PW_{12} , P-UCNS, and PW_{12} -P-UCNS with varying PW_{12} loading were also tested (The corresponding characterization results can be seen in Figs. S5–S7).

Fig. 6(a) shows the activity of PW_{12} , P-UCNS, and PW_{12} -P-UCNS towards the selective benzyl alcohol oxidation under Xe lamp illumination. A blank experiment without photocatalyst was also performed under the same conditions, and the results showed that the reaction without PW_{12} -P-UCNS, under irradiation, for 2 h, barely proceeds. The adsorption of reactants on as-prepared photocatalysts was also considered, by initially leaving the catalytic system in the dark, under stirring, for 0.5 h. After illumination for 2 h, the order of photo-oxidation activity follows the order of PW_{12} -P-UCNS > P-UCNS > PW_{12} . Obviously, the as-prepared PW_{12} -P-UCNS photocatalyst exhibits the highest photocatalytic oxidation activity, reaching benzyl alcohol conversion of 58.3% and benzaldehyde selectivity of 99.5%. The influence of PW_{12} loading of PW_{12} -P-UCNS on photocatalytic oxidation activity was also researched. As shown in Fig. 6(b), increasing PW_{12} loading leads to an increase of the conversion to benzyl alcohol, while the selectivity to benzaldehyde markedly decreases. In order to obtain high conversion to benzyl alcohol and selectivity to benzaldehyde, PW_{12} -P-UCNS with 34.8 wt% PW_{12} loading was selected for subsequent photocatalytic tests with comprehensive consideration of conversion-to-benzyl alcohol and selectivity-to-benzaldehyde (Fig. S8). Moreover, the oxidation activity of as-prepared PW_{12} -P-UCNS was compared with the reported value in literature and exhibited excellent catalytic performance (Table S1). The prepared PW_{12} -P-UCNS shows the following competitive advantages: ① the solvent of catalytic system is water, making the process green, eco-friendly and sustainable; ② high target product selectivity and reactant conversion obtained under mild reaction conditions (short reaction time and low reaction temperature); ③ high stability and inexpensive production compared to noble metals.

3.6. Photocatalyst reusability

The regeneration and reusability of photocatalysts are considered as two key issues to evaluate catalytic performance. Herein, the reusability of as-prepared PW_{12} -P-UCNS was evaluated by catalysing the oxidation of benzyl alcohol for five consecutive cycles. As shown in Fig. 7(a), after five consecutive cycles, the benzaldehyde selectivity is retained almost as high as in the original performance, whereas the benzyl alcohol conversion shows a slight decrease after three cycles. In order to investigate the cause of

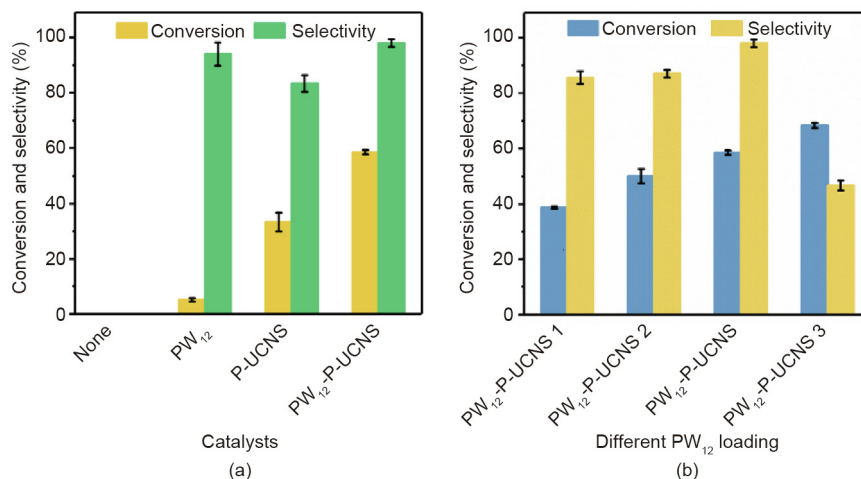


Fig. 6. The catalytic performance of (a) various photocatalysts and (b) PW₁₂-P-UCNS with different PW₁₂ loading towards the benzyl alcohol conversion and benzaldehyde selectivity in deionized water. Reaction conditions: 20 mg catalysts, 10 mL deionized water, 0.1 mmol benzyl alcohol, and 2 h Xe lamp irradiation.

activity loss, we initially performed inductively coupled plasma atomic emission spectrometry (ICP-AES) analysis using the reaction liquid after separating the photocatalyst, to identify whether PW₁₂ is leaching in the catalytic system. Based on tungsten content results, it can be confirmed that leaching of PW₁₂ species hardly occurs in the examined reaction system. Furthermore, structural and morphological information of the used PW₁₂-P-UCNS catalyst was obtained using FT-IR, XRD, and TEM. As can be seen in Fig. 7 (b), the used PW₁₂-P-UCNS catalyst exhibits thin flaky nanostructure. Moreover, the characteristic signals ascribed to the Keggin units of PW₁₂ can still be found and there is no obvious structural

change in Fig. 7(d). These results suggest that the activity loss of PW₁₂-P-UCNS after five consecutive cycles could be attributed to the mass loss of photocatalyst during recycling, although for at least five consecutive cycles, the as-prepared PW₁₂-P-UCNS does not show any morphological or structural change.

3.7. Photocatalytic mechanism

The behaviors of photogenerated electron-hole pairs can be monitored by testing their photoelectrochemical properties [4]. Initially, the separation and transfer efficiency of the photogener-

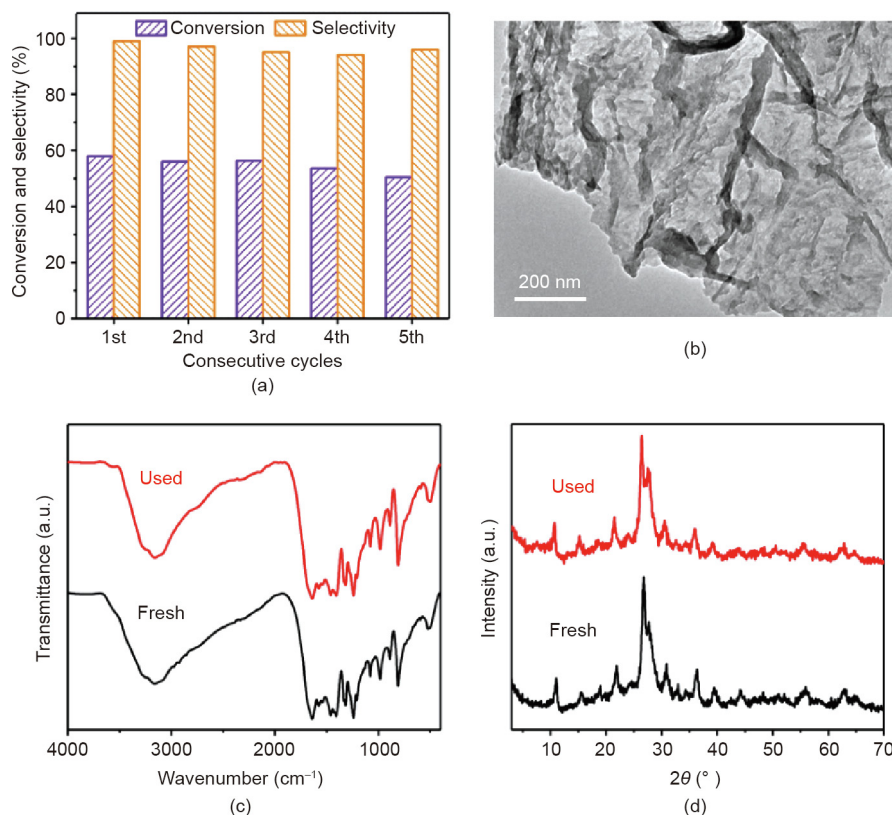


Fig. 7. (a) Reusability; (b) the image of TEM; (c) spectra of FT-IR; and (d) spectra of XRD towards fresh and used PW₁₂-P-UCNS photocatalyst. Reaction conditions: 20 mg catalysts, 10 mL deionized water, 0.1 mmol benzyl alcohol, and 2 h Xe lamp irradiation.

ated charge carriers towards the as-prepared P-UCNS and PW₁₂-P-UCNS photocatalysts was evaluated using transient photocurrent measurement. As shown in Fig. 8(a), the photocurrent responses of P-UCNS and PW₁₂-P-UCNS can be reproduced and are stable over a period of five illumination cycles. It was found that PW₁₂-P-UCNS (2.52 μ A) showed a 3.8-fold enhancement in the photocurrent intensity compared with P-UCNS (0.66 μ A). This indicates the much-improved separation and transfer efficiency for photogenerated electrons and holes, attributed to the incorporation of PW₁₂ species. The incorporated PW₁₂ functions as superior electron acceptors, restricting the recombination of photogenerated electrons and holes. Moreover, the intensity of the photoluminescence (PL) spectra emission spectra indicates the recombination rate of photogenerated electron-hole pairs. As shown in Fig. S9, the as-prepared PW₁₂-P-UCNS exhibited the lowest radiation recombination rate of photogenerated carriers compared with g-C₃N₄, UCNS and P-UCNS, which was consistent with the results obtained from transient photocurrent measurement.

Subsequently, the separation efficiency of the photogenerated electrons and holes was investigated using electrochemical impedance spectroscopy (EIS) measurements [2]. The high-frequency semicircle in the Nyquist plot represents the charge-transfer procedure, whose radius reflects the charge-transfer resistance [42,43]. The smaller radius of semicircle indicates the smaller charge transfer resistance. The as-prepared PW₁₂-P-UCNS showed smaller radius of curvature compared with P-UCNS, implying higher charge separation efficiency (Fig. 8(b)). The above results show that the charge separation efficiency and resistance of charge

transfer of photocatalyst were greatly improved after the incorporation of PW₁₂.

In order to investigate the potential mechanism of PW₁₂-P-UCNS nanocomposite for selective alcohol oxidation, we examined the main active species in the reaction by the 5,5-dimethyl-1-pyrroline-*N*-oxide (DMPO) spin-trapping electron spin resonance (ESR) measurements. As shown in Fig. 9(a), there was no obvious signal without light irradiation. Under solar light and the presence of PW₁₂-P-UCNS photocatalyst, there were characteristic signals with 1:1:1:1 of intensity ratio in methanol dispersion, which can be assigned to the DMPO- \cdot O₂⁻ adduct [44]. This indicates that \cdot O₂⁻ can be formed in the photocatalytic course upon irradiation.

The effect of different active species on the model reaction was carefully investigated by using potassium persulfate (K₂S₂O₈) as electron scavengers, oxalic acid (C₂H₂O₄) as hole scavengers, 1,4-benzoquinone (BQ) as \cdot O₂⁻ scavengers, and tertbutyl alcohol (TBA) as \cdot O₂⁻ scavengers [1,2,5,45]. As shown in Fig. 9(b), when C₂H₂O₄ or BQ was introduced, the conversion of benzyl alcohol rapidly declined, demonstrating that \cdot O₂⁻ and holes were important active moieties in the current oxidation system. Meanwhile, the decrease of conversion-to-benzyl alcohol in the TBA-added photocatalytic system was negligible, implying that \cdot O₂⁻ radicals showed no vital role during the current photocatalytic reaction process. Furthermore, it was found that conversion-to-benzyl alcohol increased slightly after adding K₂S₂O₈. This suggested that the addition of electron scavenger increased greatly the consumption of electrons, thus increasing the amount of active holes on PW₁₂-P-UCNS and improving the indirect hole oxidation of benzyl alcohol on the surface [1].

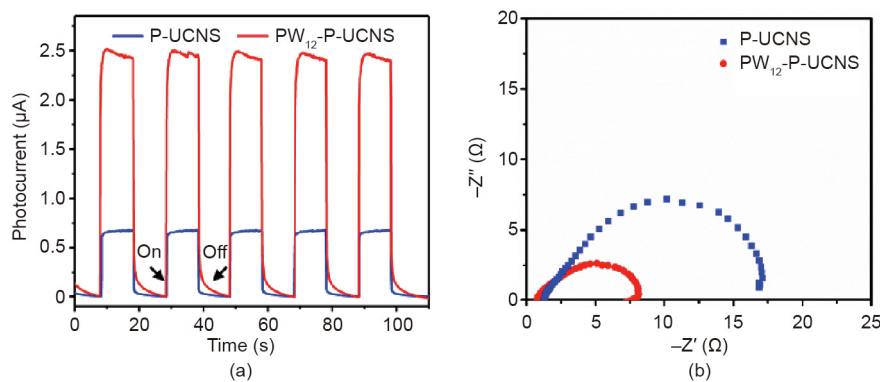


Fig. 8. Profiles of (a) photocurrent-time and (b) electrochemical impedance spectroscopy (EIS) measurement. $-Z''$: negative imaginary impedance; Z' : real impedance.

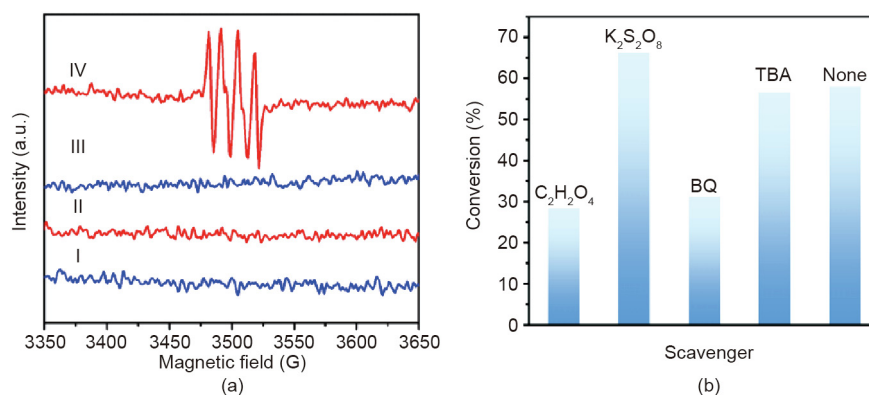


Fig. 9. (a) The DMPO spin-trapping ESR spectra of PW₁₂-P-UCNS. I. DMPO in dark; II. PW₁₂-P-UCNS in dark; III. DMPO-Xe lamp; VI. PW₁₂-P-UCNS-Xe lamp. (b) The results of different scavengers in the PW₁₂-P-UCNS-photocatalytic benzyl alcohol oxidation.

Therefore, it was proven that $h\nu_{VB}^+$ and $\cdot O_2^-$ were the main active moieties for the examined oxidation system under solar light illumination.

In order to estimate the relative positions of CB and VB of PW_{12} and P-UCNS, we calculated the optical band gap, CV, and measured the flat band potential (Fig. S10). Based on the above results, the conventional Type II-Heterojunction and direct Z-scheme mechanism can be used to describe the current catalytic system.

If the as-prepared PW_{12} -P-UCNS followed the Type II-Heterojunction mechanism, the electrons in the CB of P-UCNS could be accumulated in the CB of PW_{12} , while the holes in the VB of PW_{12} could transfer to the VB of P-UCNS. As shown in Fig. S11, the CB level of PW_{12} (+0.30 V vs. NHE, determined by CV, NHE is the normal hydrogen electrode, Fig. S10) was more positive than the redox potential of $O_2/\cdot O_2^-$ (-0.33 V vs. NHE) [28,46], which was hardly to reduce O_2 to $\cdot O_2^-$ radicals directly. In addition, the holes on the VB of P-UCNS were also unable to generate $\cdot O_2^-$ radicals. The above Type II-Heterojunction mechanism conflicted with the results of ESR. Therefore, a light-driven Z-scheme was proposed instead, to describe the system.

As illustrated in Fig. 10, a reasonable mechanism of PW_{12} -P-UCNS selectively photocatalyzed benzyl alcohol oxidation to produce benzaldehyde was revealed. The electron-hole pairs are generated after irradiation of the PW_{12} -P-UCNS (Eq. (1)). Because of the close integration between PW_{12} and P-UCNS as well as well-matched energy band structure, the initial transfer of electrons from the CB of the PW_{12} species to the VB of P-UCNS was facilitated, and thus they could further realize the recombination with the holes on the VB of P-UCNS. During the Z-scheme-driven photo-oxidation process of benzyl alcohol, the benzyl alcohol cation radicals ($C_6H_5CH_2OH^{+\bullet}$) were initially produced by the holes on the VB of PW_{12} (Eq. (2)). Meanwhile, the electrons of P-UCNS are more likely to be scavenged by molecular oxygen to produce more abundant $\cdot O_2^-$ radicals (-0.33 V vs. NHE) (Eq. (3)), which benefits the modification of phosphoric acid and thereby improves the adsorption of O_2 on the surface of P-UCNS [13,28,46]. Lastly, the activated intermediates further react with produced $\cdot O_2^-$ to generate the targeted benzaldehyde (Eq. (4)).

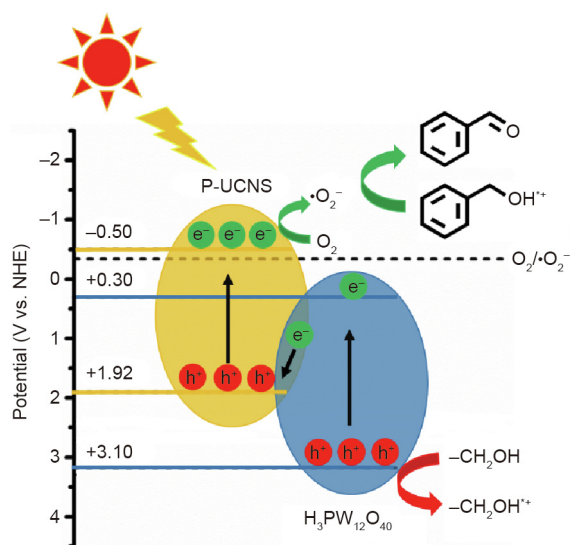
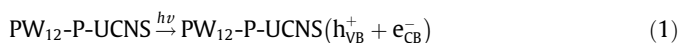


Fig. 10. The proposed mechanism for the PW_{12} -P-UCNS-catalysed benzyl alcohol photo-oxidation under the current catalytic system.



On the other hand, as-prepared PW_{12} -P-UCNS photocatalyst can act as the H-bonding acceptor because of the C-N-H, C-OH, and POMs species present on the surface. Accordingly, the surface of PW_{12} -P-UCNS photocatalysts prefers to adsorb the reactants via H-bonding or electrostatic interaction, leading to the high benzyl alcohol conversion. Meanwhile, the weak interaction between benzaldehyde and PW_{12} -P-UCNS makes the former desorb quickly from the surface, avoiding the over-oxidation of the target product and thereby obtaining high selectivity of benzaldehyde. Such a Z-scheme-driven photocatalysed oxidation reaction shows excellent benzyl alcohol conversion and benzaldehyde selectivity attributed to the sharp separation of photogenerated electron-hole pairs and abundance of active species of $\cdot O_2^-$ radicals. Based on the aforementioned results, as-prepared PW_{12} -P-UCNS can be used as an effective and environmentally benign photocatalyst for the chosen oxidation reaction.

4. Conclusion

To summarise, an efficient and environmentally friendly photocatalyst (PW_{12} -P-UCNS) was successfully constructed by immobilising PW_{12} on $g\text{-}C_3N_4$ nanosheets modified using phosphoric acid. The as-prepared PW_{12} -P-UCNS photocatalyst showed excellent photocatalytic performance including its activity and stability in selective benzyl alcohol oxidation to produce benzaldehyde, i.e. 58.3% conversion of benzyl alcohol and 99.5% selectivity to benzaldehyde within 2 h. Careful investigation of the photoelectrochemical properties, including photocurrent, scavenger experiments and ESR measurement, such a Z-scheme-driven catalytic performance can be assigned to the following facts. Firstly, the incorporated Keggin units facilitate the spontaneous migration of electrons, and thereby accelerate interfacial charge carrier separation; Secondly, more abundant $\cdot O_2^-$ radicals (the detected main active species during the current selective photo-oxidation reaction process) are generated, which is beneficial from the improvement of O_2 adsorption on the surface of P-UCNS. Based on the aforementioned results and observations, the PW_{12} -P-UCNS photocatalysts show great potential for driving chemical oxidation reactions using sunlight.

Declaration of Competing Interest

The authors declare that they have no known competing financial interests or personal relationships that could have appeared to influence the work reported in this paper.

Acknowledgements

This research was supported by the National Nature Science Foundation of China (21625101, 21521005, and 21808011), the National Key Research and Development Program of China (2017YFB0307303), Beijing Natural Science Foundation (2202039) and the Fundamental Research Funds for the Central Universities (XK1802-6, XK1902, and 12060093063).

Appendix A. Supplementary data

Supplementary data to this article can be found online at <https://doi.org/10.1016/j.eng.2020.07.025>.

References

- [1] Su Y, Han Z, Zhang L, Wang W, Duan M, Li X, et al. Surface hydrogen bonds assisted meso-porous WO₃ photocatalysts for high selective oxidation of benzylalcohol to benzylaldehyde. *Appl Catal B* 2017;217():108–14.
- [2] Xiao CL, Zhang L, Hao HC, Wang WZ. High selective oxidation of benzyl alcohol to benzylaldehyde and benzoic acid with surface oxygen vacancies on W₁₈O₄₉/holey ultrathin g-C₃N₄ nanosheets. *ACS Sustainable Chem Eng* 2019;7(7):7268–76.
- [3] Xing MY, Qiu BC, Du MM, Zhu QH, Wang LZ, Zhang JL. Spatially separated CdS shells exposed with reduction surfaces for enhancing photocatalytic hydrogen evolution. *Adv Funct Mater* 2017;27(35):1702624.
- [4] Xiao X, Zheng CX, Lu ML, Zhang L, Liu F, Zuo XX, et al. Deficient Bi₂₄O₃₁Br₁₀ as a highly efficient photocatalyst for photocatalytic oxidation of benzyl alcohol to benzaldehyde under blue LED irradiation. *Appl Catal B* 2018;228:142–51.
- [5] Yang X, Zhao H, Feng J, Chen Y, Gao S, Cao R. Visible-light-driven selective oxidation of alcohols using a dye-sensitized TiO₂-polyoxometalate catalyst. *J Catal* 2017;351:59–66.
- [6] Chen ZM, Wang JG, Zhai GJ, An W, Men Y. Hierarchical yolk-shell WO₃ microspheres with highly enhanced photoactivity for selective alcohol oxidations. *Appl Catal B* 2017;218:825–32.
- [7] Chen YZ, Wang ZU, Wang H, Lu J, Yu SH, Jiang HL. Singlet oxygen-engaged selective photo-oxidation over Pt nanocrystals/porphyrinic MOF: the roles of photothermal effect and Pt electronic state. *J Am Chem Soc* 2017;139(5):2035–44.
- [8] Sun XS, Luo X, Zhang XD, Xie JF, Jin S, Wang H, et al. Enhanced superoxide generation on defective surfaces for selective photooxidation. *J Am Chem Soc* 2019;141(9):3797–801.
- [9] Derikvand H, Nezamzadeh-Ejhiieh A. Increased photocatalytic activity of NiO and ZnO in photodegradation of a model drug aqueous solution: effect of coupling, supporting, particles size and calcination temperature. *J Hazard Mater* 2017;321:629–38.
- [10] R  ther T, Bond AM, Jackson WR. Solar light induced photocatalytic oxidation of benzyl alcohol using heteropolyoxometalate catalysts of the type [S₂M₁₈O₆₂]⁴⁻. *Green Chem* 2003;5(4):364–6.
- [11] Gao SY, Cao R, L   J, Li GL, Li YF, Yang HX. Photocatalytic properties of polyoxometalate-thionine composite films immobilized onto microspheres under sunlight irradiation. *J Mater Chem* 2009;19(24):4157–63.
- [12] Meng JQ, Wang XY, Yang X, Hu A, Guo YH, Yang YX. Enhanced gas-phase photocatalytic removal of aromatics over direct Z-scheme-dictated H₃PW₁₂O₄₀/g-C₃N₄ film-coated optical fibers. *Appl Catal B* 2019;251:168–80.
- [13] Xiao CL, Zhang L, Wang KF, Wang HP, Zhou YY, Wang WZ. A new approach to enhance photocatalytic nitrogen fixation performance via a phosphate-bridge: a case study of SiW₁₂/K-C₃N₄. *Appl Catal B* 2018;239:260–7.
- [14] Liu JH, Zhang TK, Wang ZC, Dawson G, Chen W. Simple pyrolysis of urea into graphitic carbon nitride with recyclable adsorption and photocatalytic activity. *J Mater Chem* 2011;21(38):14398–401.
- [15] Zhang YJ, Thomas A, Antonietti M, Wang XC. Activation of carbon nitride solids by protonation: morphology changes, enhanced ionic conductivity, and photoconduction experiments. *J Am Chem Soc* 2009;131(1):50–1.
- [16] Du XR, Zou GJ, Wang ZH, Wang XL. A scalable chemical route to soluble acidified graphitic carbon nitride: an ideal precursor for isolated ultrathin g-C₃N₄ nanosheets. *Nanoscale* 2015;7(19):8701–6.
- [17] Wang HF, Zhao M, Zhao Q, Yang YF, Wang CY, Wang YJ. *In-situ* immobilization of H₃PMo₁₀V₂O₄₀ on protonated graphitic carbon nitride under hydrothermal conditions: a highly efficient and reusable catalyst for hydroxylation of benzene. *Ind Eng Chem Res* 2017;56(10):2711–21.
- [18] Ou HH, Tang C, Chen XR, Zhou M, Wang XC. Solvated electrons for photochemistry syntheses using conjugated carbon nitride polymers. *ACS Catal* 2019;9(4):2949–55.
- [19] Yu HJ, Shi R, Zhao YX, Bian T, Zhao YF, Zhou C, et al. Alkali-assisted synthesis of nitrogen deficient graphitic carbon nitride with tunable band structures for efficient visible-light-driven hydrogen evolution. *Adv Mater* 2017;29(16):1605148.
- [20] Liu HF, Li HJ, Lu JM, Zeng S, Wang M, Luo NC, et al. Photocatalytic cleavage of C-C bond in lignin models under visible light on mesoporous graphitic carbon nitride through π - π stacking interaction. *ACS Catal* 2018;8(6):4761–71.
- [21] Gao HH, Yang HC, Xu JZ, Zhang SW, Li JX. Strongly coupled g-C₃N₄ nanosheets-Co₃O₄ quantum dots as 2D/0D heterostructure composite for peroxymonosulfate activation. *Small* 2018;14(31):1801353.
- [22] Wang WJ, Xu P, Chen M, Zeng GM, Zhang C, Zhou CY, et al. Alkali metal-assisted synthesis of graphite carbon nitride with tunable band-gap for enhanced visible-light-driven photocatalytic performance. *ACS Sustainable Chem Eng* 2018;6(11):15503–16.
- [23] Zhu JJ, Xiao P, Li HL, Carabineiro SAC. Graphitic carbon nitride: synthesis, properties, and applications in catalysis. *ACS Appl Mater Interfaces* 2014;6(19):16449–65.
- [24] Yang SB, Gong YJ, Zhang JS, Zhan L, Ma LL, Fang ZY, et al. Exfoliated graphitic carbon nitride nanosheets as efficient catalysts for hydrogen evolution under visible light. *Adv Mater* 2013;25(17):2452–6.
- [25] Lin QY, Li L, Liang SJ, Liu MH, Bi JH, Wu L. Efficient synthesis of monolayer carbon nitride 2D nanosheet with tunable concentration and enhanced visible-light photocatalytic activities. *Appl Catal B* 2015;163:135–42.
- [26] Xu YG, Xu H, Wang L, Yan J, Li HM, Song YH, et al. The CNT modified white C₃N₄ composite photocatalyst with enhanced visible-light response photoactivity. *Dalton Trans* 2013;42(21):7604–13.
- [27] Huang CH, Zhang WM, Yan ZM, Gao J, Liu W, Tong P, et al. Protonated mesoporous graphitic carbon nitride for rapid and highly efficient removal of microcystins. *RSC Adv* 2015;5(56):45368–75.
- [28] Liu C, Jing LQ, He LM, Luan YB, Li CM. Phosphate-modified graphitic C₃N₄ as efficient photocatalyst for degrading colorless pollutants by promoting O₂ adsorption. *Chem Commun* 2014;50(16):1999–2001.
- [29] Li KX, Yan LS, Zeng ZX, Luo SL, Luo XB, Liu XM, et al. Fabrication of H₃PW₁₂O₄₀-doped carbon nitride nanotubes by one-step hydrothermal treatment strategy and their efficient visible-light photocatalytic activity toward representative aqueous persistent organic pollutants degradation. *Appl Catal B* 2014;156–157:141–52.
- [30] Zhang WX, Cui JC, Tao CA, Wu YG, Li ZP, Ma L, et al. A strategy for producing pure single-layer graphene sheets based on a confined self-assembly approach. *Angew Chem Int Ed* 2009;48(32):5864–8.
- [31] Sun YH, Meng PC, Liu X. Self-assembly of tungstophosphoric acid/acidified carbon nitride hybrids with enhanced visible-light-driven photocatalytic activity for the degradation of imidacloprid and acetamiprid. *Appl Surf Sci* 2018;456:259–69.
- [32] Ma TY, Tang YH, Dai S, Qiao SZ. Proton-functionalized two-dimensional graphitic carbon nitride nanosheet: an excellent metal-/label-free biosensing platform. *Small* 2014;10(12):2382–9.
- [33] Han C, Wang YD, Lei YP, Wang B, Wu N, Shi Q, et al. *In situ* synthesis of graphitic-C₃N₄ nanosheet hybridized N-doped TiO₂ nanofibers for efficient photocatalytic H₂ production and degradation. *Nano Res* 2015;8(4):1199–209.
- [34] Ong WJ, Putri LK, Tan LL, Chai SP, Yong ST. Heterostructured AgX/g-C₃N₄ (X = Cl and Br) nanocomposites via a sonication-assisted deposition-precipitation approach: emerging role of halide ions in the synergistic photocatalytic reduction of carbon dioxide. *Appl Catal B* 2016;180:530–43.
- [35] Yang XL, Qian FF, Zou GJ, Li ML, Lu JR, Li YM, et al. Facile fabrication of acidified g-C₃N₄/g-C₃N₄ hybrids with enhanced photocatalysis performance under visible light irradiation. *Appl Catal B* 2016;193:22–35.
- [36] Subudhi S, Mansingh S, Swain G, Behera A, Rath D, Parida K. HPW-Anchored UiO-66 metal-organic framework: a promising photocatalyst effective toward tetracycline hydrochloride degradation and H₂ evolution via Z-scheme charge dynamics. *Inorg Chem* 2019;58(8):4921–34.
- [37] Meng PC, Heng HM, Sun YH, Huang JH, Yang JP, Liu X. Positive effects of phosphotungstic acid on the *in-situ* solid-state polymerization and visible light photocatalytic activity of polyimide-based photocatalyst. *Appl Catal B* 2018;226:487–98.
- [38] Cai JS, Huang JY, Wang SC, Iocozzia J, Sun ZT, Sun JY, et al. Crafting mussel-inspired metal nanoparticle-decorated ultrathin graphitic carbon nitride for the degradation of chemical pollutants and production of chemical resources. *Adv Mater* 2019;31(15):1806314.
- [39] Wang Y, Wang XC, Antonietti M. Polymeric graphitic carbon nitride as a heterogeneous organocatalyst: from photochemistry to multipurpose catalysis to sustainable chemistry. *Angew Chem Int Ed* 2012;51(1):68–89.
- [40] Jiang LB, Yuan XZ, Zeng GM, Liang J, Chen XH, Yu HB, et al. *In-situ* synthesis of direct solid-state dual Z-scheme WO₃/g-C₃N₄/Bi₂O₃ photocatalyst for the degradation of refractory pollutant. *Appl Catal B* 2018;227:376–85.
- [41] Babaahmadi-Milani M, Nezamzadeh-Ejhiieh A. A comprehensive study on photocatalytic activity of supported Ni/Pb sulfide and oxide systems onto natural zeolite nanoparticles. *J Hazard Mater* 2016;318:291–301.
- [42] Liang FF, Zhu YF. Enhancement of mineralization ability for phenol via synergetic effect of photoelectrocatalysis of g-C₃N₄ film. *Appl Catal B* 2016;180:324–9.
- [43] Yang PJ, Ou HH, Fang YX, Wang XC. A facile steam reforming strategy to delaminate layered carbon nitride semiconductors for photoredox catalysis. *Angew Chem Int Ed* 2017;56(14):3992–6.
- [44] Du XD, Zhang YQ, Hussain I, Huang SB, Huang WL. Insight into reactive oxygen species in persulfate activation with copper oxide: activated persulfate and trace radicals. *Chem Eng J* 2017;313:1023–32.
- [45] Sun LQ, Li B, Chu XY, Sun N, Qu Y, Zhang XL, et al. Synthesis of Si-O-bridged g-C₃N₄/WO₃ 2D-heterojunctional nanocomposites as efficient photocatalysts for aerobic alcohol oxidation and mechanism insight. *ACS Sustainable Chem Eng* 2019;7(11):9916–27.
- [46] Chu MN, Hu K, Wang JS, Liu YD, Ali S, Qin CL, et al. Synthesis of g-C₃N₄-based photocatalysts with recyclable feature for efficient 2,4-dichlorophenol degradation and mechanisms. *Appl Catal B* 2019;243:57–65.